JOURNAL OF COMPUTATIONAL PHYSICS 51, 28–64 (1983)

Rayleigh–Taylor Instability and the Use of Conformal Maps for Ideal Fluid Flow

RALPH MENIKOFF AND CHARLES ZEMACH

Theoretical Division, Los Alamos National Laboratory, Los Alamos, New Mexico 87545

Received July 21, 1982

Potential theory permits ideal fluid dynamics to be formulated in terms of boundary motion. In two dimension, the flow can then be found using conformal mapping. The evolution of some Rayleigh–Taylor instabilities is calculated well into the large amplitude nonlinear regime. The Rayleigh–Taylor calculation for Atwood ratio unity is used as a prototype for a system of theoretical and numerical techniques exploiting complex variable theory and high-order quadrature methods.

I. INTRODUCTION

We consider the idealized case of incompressible, irrotational, inviscid fluid flow in plane geometry. With the use of potential theory the time development of the flow can be reduced to the problem of the motion of the fluid interface [1]. The potential problem can be solved by the use of conformal maps.

We apply this method to Rayleigh–Taylor instability which occurs when a light fluid accelerates a heavy fluid. For small disturbances, the amplitude of the interface initially grows exponentially in accordance with the linear theory [2]. Subsequently, nonlinear effects become important and the interface develops into a shape with a rising and broadening bubble of the light fluid and a falling and narrowing spike of the heavy fluid.

We have performed numerical calculations for a simplified case of a single semi-infinite fluid falling under gravity (free fall of a free surface) with an initial single frequency periodic disturbance. This case allows us to isolate and concentrate on the behavior of a single boundary. For a single fluid there is a pure Rayleigh–Taylor instability without the subsequent development of a Kelvin–Helmholtz instability. We calculate the evolution of the interface into the large amplitude regime. The flow asymptotically approaches a steady state in which the bubble rises with a constant velocity and the spike is in free fall. Similar calculations have been described in [3]. In addition, this problem has been calculated using the vortex method in [4].

A more general purpose in this work was to explore and test various mathematical and numerical techniques for dealing with moving boundary problems in two dimensions. A partial list of these includes:

0021-9991/83 $3.00

(a) numerical conformal mapping to high accuracy, applicable to regions with severely distorted boundaries, requiring short computer times,

(b) quadratures of Gauss type for the singular integrals characteristic of Green's function representations,

(c) numerical derivatives through Gauss quadrature techniques, and

(d) partial fractions modeling of harmonic functions and analytic functions of a complex variable derived from discrete numerical boundary data. This is efficient not only for evaluation of such functions within the region, but also for calculations with them that can be done analytically.

The mathematical formulation of the fluid flow in terms of the motion of the boundary is described in Section II. The application of conformal maps to solve the potential problem is described in Section III. The differencing scheme for the equations used in the numerical calculations is described in Section IV. The results of the numerical calculations are given in Section V. Concluding remarks are given in Section VI. The properties of the steady state solution for the Rayleigh–Taylor problem are described in the Appendix.

II. Mathematical Formulation

A. *Definitions*

Two semi-infinite fluids occupy a two-dimensional space and are separated by a one-dimensional interface. Coordinates x and y label the horizontal and vertical axes, respectively. The fluids are subject to a potential energy per unit mass $V(x, y)$. For the Rayleigh–Taylor problem

$$V(x, y) = gy, \tag{2.1}$$

where g is the acceleration of gravity.

If the fluids are motionless and the interface is flat and horizontal, then the system is held in static equilibrium. At $t = 0$, the system is perturbed from equilibrium. We wish to follow the subsequent motions of the interface and the fluids.

Let ρ, $\phi(x, y, t)$, $\mathbf{v}(x, y, t) = \nabla\phi$, $P(x, y, t)$ be the density, velocity potential, velocity, and pressure for the upper fluid, and let $\bar{\rho}$, $\bar{\phi}(x, y, t)$, etc. denote the same variables for the lower fluid. Because the fluids are incompressible, the potentials are harmonic functions. In addition, we assume there is no fluid motion remote from the interface. Hence, the gradients of the potentials go to zero as $y \to \pm\infty$.

Let the interface at time t be specified by

$$x = \hat{x}(\alpha, t), \qquad y = \hat{y}(\alpha, t) \tag{2.2}$$

in terms of a continuous parameter α. Partial differentiation with respect to t and α

will be denoted by subscripts. Let **n** and **s** be unit normal and unit tangent vectors to (2.2)

$$\mathbf{n} = (-\hat{y}_\alpha, \hat{x}_\alpha)/(\hat{x}_\alpha^2 + \hat{y}_\alpha^2)^{1/2}, \tag{2.3a}$$

$$\mathbf{s} = (\hat{x}_\alpha, \hat{y}_\alpha)/(\hat{x}_\alpha^2 + \hat{y}_\alpha^2)^{1/2}. \tag{2.3b}$$

As the interface is traversed in the direction of increasing α, we suppose the upper fluid is on the left; then **n** points into the upper fluid. With v_n, v_s denoting the velocity components in directions **n** and **s** for a fluid element on the interface labeled by α, we have

$$\hat{x}_t = (-\hat{y}_\alpha v_n + \hat{x}_\alpha v_s)/(\hat{x}_\alpha^2 + \hat{y}_\alpha^2)^{1/2}, \tag{2.4a}$$

$$\hat{y}_t = (\hat{x}_\alpha v_n + \hat{y}_\alpha v_s)/(\hat{x}_\alpha^2 + \hat{y}_\alpha)^{1/2}. \tag{2.4b}$$

For the potentials and fluid velocity components of the interface, we adopt the abbreviated notation

$$F(\alpha, t) = \phi(x, y, t), \qquad \bar{F}(\alpha, t) = \phi(x, y, t), \tag{2.5a}$$

$$F_n(\alpha, t) = \mathbf{n} \cdot \underline{\nabla}\phi(x, y, t), \qquad \bar{F}_n(\alpha, t) = \mathbf{n} \cdot \underline{\nabla}\bar{\phi}, \tag{2.5b}$$

$$F_s(\alpha, t) = \mathbf{s} \cdot \underline{\nabla}\phi(x, y, t), \qquad \bar{F}_s(\alpha, t) = \mathbf{s} \cdot \underline{\nabla}\bar{\phi}, \tag{2.5c}$$

at $x = \hat{x}(\alpha, t)$, $y = \hat{y}(\alpha, t)$.

B. *Kinematic Equation*

The motion of the interface must be consistent with the normal motion of the fluids. Thus,

$$v_n = F_n = \bar{F}_n. \tag{2.6}$$

Because we are considering inviscid flow, the fluids can slip relative to one another parallel to the interface. There is a shear or vortex at the interface. The velocity v_s is arbitrary and represents the freedom to choose the parameterization of the interface. This is discussed in more detail in Section IV.

C. *Equations of Motion*

From the Bernoulli equation

$$\phi_t = -\tfrac{1}{2}(\nabla\phi)^2 - gy - P/\rho \tag{2.7}$$

and the time derivative of (2.5a) we obtain, on the interface,

$$F_t = \tfrac{1}{2}(F_n^2 - F_s^2 + 2v_s F_s) - g\hat{y} - P/\rho. \tag{2.8a}$$

Similarly, for the lower fluid

$$\bar{F}_t = \tfrac{1}{2}(\bar{F}_n^2 - \bar{F}_s^2 + 2v_s\bar{F}_s) - g\hat{y} - \bar{P}/\bar{\rho}. \tag{2.8b}$$

The effect of a surface tension σ may be included by setting the pressure difference across the interface to be

$$P - \bar{P} = \sigma/R, \tag{2.9}$$

where R is the radius of curvature

$$R^{-1} = (\hat{x}_\alpha \hat{y}_{\alpha\alpha} - \hat{y}_\alpha \hat{x}_{\alpha\alpha})/(\hat{x}_\alpha^2 + \hat{y}_\alpha^2)^{3/2}. \tag{2.10}$$

D. *Interface Equations*

Let $\tilde{F}(\alpha(t))$ stand for a "mixed" boundary value

$$\tilde{F}(\alpha, t) = \rho F(\alpha, t) - \bar{\rho}\bar{F}(\alpha, t). \tag{2.11}$$

Then eliminating the pressure from Eqs. (2.8a) and (2.8b), we get

$$\begin{aligned}\tilde{F}_t(\alpha, t) = {} & \tfrac{1}{2}\rho(F_n^2 - F_s^2 + 2v_sF_s) - \tfrac{1}{2}\bar{\rho}(\bar{F}_n^2 - \bar{F}_s^2 + 2v_s\bar{F}_s) \\ & - (\rho - \bar{\rho})\, g\hat{y} - \sigma/R,\end{aligned} \tag{2.12}$$

which is the basic dynamical equation for the fluid motion. The potentials as harmonic functions are determined from their boundary data by means of linear integral equations with Green's function kernels. These Green's functions are given in the next section in terms of conformal maps. On the interface we can infer relations of the form (with K, $\bar{K}$ denoting linear integral operators; see Eq. (3.8))

$$F_s = K[F_n], \qquad \bar{F}_s = \bar{K}[\bar{F}_n] = \bar{K}[\bar{F}_n] \tag{2.13}$$

and hence, for the tangential derivative of $\tilde{F}(\alpha, t)$, we have

$$\tilde{F}_s = (\rho K - \bar{\rho}\bar{K})[F_n]. \tag{2.14}$$

The two-dimensional problem can now be formulated in terms of functions on the interface. The three primary functions to be determined are $\hat{x}(\alpha, t)$, $\hat{y}(\alpha, t)$, and $\tilde{F}(\alpha, t)$. First, the α-parameterization scheme is specified so that v_s can be expressed in terms of the other functions. Second, $\tilde{F}_s(\alpha, t)$ is found from $\tilde{F}(\alpha, t)$ via differentiation of $\tilde{F}$, $\hat{x}$, and $\hat{y}$ with respect to α. Then v_n is found by inverting Eq. (2.14). (In the one fluid case, e.g., $\bar{\rho} = 0$, Eq. (2.14) can be inverted analytically to give v_n as a quadrature over $\tilde{F}_s$.) Finally, F_s and $\bar{F}_s$ are obtained by quadrature of Eq. (2.13). Thus, the ingredients to calculate the time derivatives of $\hat{x}$, $\hat{y}$, and F from Eqs. (2.4) and (2.12) are all in hand. In Section III we describe how complex variable theory can be used to determine the Green's function kernels and also determine the hydrodynamic variables in the interior from the boundary data.

III. Application of Complex Variable Theory

A. *Preliminaries*

We must do numerical calculations of (1) Green's functions for regions with irregular boundaries, and (2) integrals with these Green's functions or their derivatives as kernels. We consider the region of the upper fluid at a fixed time; the procedure for the lower fluid is similar.

The x, y plane may be regarded as the complex z plane; $z = x + iy$. Let there be a conformal mapping between the region of the upper fluid and a "standard" region of the complex w plane, $w = u + iv$. Green's functions in two dimensions for the Laplace equation are invariant under such maps. The determinations of Green's function for the fluid region is thus reduced to the calculation of a mapping to a standard region for which Green's function is known.

The integrals may have logarithmic singularities, or pole singularities to be evaluated as principal values. If the standard region has suitable translation symmetry, Green's function will obey certain integral identities. These can be exploited to perform subtractions in the singular integrals which regularize the integrals and permit use of high-order Gaussian quadrature rules.

We have previously described [5] efficient numerical methods for computing conformal maps and computing integrals for potential theory problems. These are applicable to the highly irregular regions that occur in Rayleigh–Taylor instability. The results needed here will now be summarized, and re-expressed to some extent in a revised notation.

We specialize to the case most frequently studied, in which the inital fluid velocities are assumed periodic in x. We may then suppose $\hat{x}(\alpha, t)$ and $\hat{y}(\alpha, t)$ periodic in α as well and take the fundamental period as $(-\pi, +\pi)$ for x and α. It should be apparent, however, how the equations below can be adapted to other geometries.

Let $z = z(w)$ map the upper half of the w plane onto the region of the upper fluid in the z plane. Assume, for standardization, that $z(w)$ maps the interval $-\pi \leqslant u \leqslant \pi$ of the u axis onto the portion of the fluid interface with $-\pi \leqslant x \leqslant \pi$. For this periodic case, the standard region is taken as the projective strip $-\pi \leqslant u \leqslant \pi$, $v \geqslant 0$. (That is, for each $v \geqslant 0$, the points $-\pi + iv$ and $\pi + iv$ are identified as the same point. The topology is such that the transformation $W = -e^{-iw}$ defines a 1–1 map from the standard region to the exterior of the unit circle in the W plane.)

Let $G(w, w')$ be Green's function for the standard region, satisfying

$$\nabla_w^2 G(w, w') = 2\pi\delta(u - u')\,\delta(v - v')$$

and

$$\partial_v G(w, w') = 0 \qquad \text{on} \quad (-\pi \leqslant u \leqslant \pi, v = 0).$$

Then

$$G(w, w') = \log|\sin \tfrac{1}{2}(w - w')| + \log|\sin \tfrac{1}{2}(w - w'^*)|. \tag{3.1}$$

To derive this, we might begin with

$$H(W, W') = \log|W - W'| + \log|W - (W'^*)^{-1}| - \log|W|.$$

This is Green's function for the exterior of the unit circle in the W plane, with zero normal-derivative boundary condition, as follows from, e.g., the method of images. Hence $G(w, w') = H(-e^{-iw}, -e^{-iw'})$ up to an arbitrary additive constant.

The standard region has translation symmetry (modulo 2π) in the horizontal direction. Thus, $G(w, w')$ depends on u and u' only through their difference. Then with subscripts again denoting partial differentiation, we have

$$\int_{-\pi}^{\pi} G_u(w, u')\, du' = -\int_{-\pi}^{\pi} G_{u'}(w, u')\, du' = 0. \tag{3.2a}$$

Also, for $w = u =$ real,

$$\int_{-\pi}^{\pi} G(u, u')\, du'/2\pi = \text{constant}, \qquad \text{independent of } u. \tag{3.2b}$$

(In this case, the constant is $-2 \log 2$.)

Consider a function $\bar{f}(w) = \bar{f}_R(u, v) + i\bar{f}_I(u, v)$ of period 2π, analytic in the standard region including the point at ∞, with

$$\lim_{v \to \infty} \bar{f}(w) = \bar{f}(\infty) = \bar{f}_R(\infty) + \bar{f}_I(\infty).$$

For example, $\bar{f}(w)$ could be the transform, $\bar{f}(w) = f[z(w)]$ of a periodic analytic function in the upper fluid region of the z plane under the conformal map. Then we have, from Green's formulas and the Cauchy–Riemann conditions,

$$\begin{aligned} \bar{f}_R(u, v) &= \bar{f}_R(\infty) + \int_{-\pi}^{\pi} G(w, u')\, \partial_{v'} \bar{f}_R(u', 0)\, du'/2\pi \\ &= \bar{f}_R(\infty) - \int_{-\pi}^{\pi} G(w, u')\, \partial_{u'} \bar{f}_I(u', 0)\, du'/2\pi. \end{aligned} \tag{3.3}$$

Integration by parts yields

$$\bar{f}_R(u, v) = \bar{f}_R(\infty) - \int_{-\pi}^{\pi} G_u(w, u')\, \bar{f}_I(u', 0)\, du'/2\pi. \tag{3.4a}$$

Similarly,

$$\bar{f}_I(u, v) = \bar{f}_I(\infty) + \int_{-\pi}^{\pi} G_u(w, u')\, \bar{f}_R(u', 0)\, du'/2\pi, \tag{3.4b}$$

where

$$G_u(w, u') = \mathrm{Re}\{\partial_u 2 \ln \sin \tfrac{1}{2}(w - u')\} = \mathrm{Re}\{\cot \tfrac{1}{2}(w - u')\}. \tag{3.5}$$

The component functions of the map $z = z(u)$ may be written

$$x = x(u, v), \qquad y = y(u, v).$$

Similarly, the component function of the inverse map $w = w(z)$ may be written

$$u = u(x, y) \qquad \text{and} \qquad v = v(x, y).$$

For the boundary points of the region, with the same parameterization as in Eq. (2.2), we can define the boundary map function

$$u(\alpha) = u(\hat{x}(\alpha, t), \hat{y}(\alpha, t))$$

whose calculation, according to the methods of [5], is the key to all other conformal map calculations. Finally, note that in terms of these definitions,

$$\hat{x}(\alpha, t) = x(u(\alpha), 0), \qquad \hat{y}(\alpha, t) = y(u(\alpha), 0).$$

B. Applications

1. *The Conformal Map*

Because $\bar{f}(w) = z(w) - w$ has the requisite analyticity and periodicity properties, we can apply Eq. (3.3) to $\bar{f}(w)$ for $v = 0$. Regularizing the integral by subtraction using Eq. (3.2b) we obtain

$$\hat{y}(\alpha, t) = y_\infty + \int_{-\pi}^{\pi} [G(u(\alpha), u(\alpha')) - G(\hat{x}(\alpha, t), \hat{x}(\alpha', t))]\, \hat{x}_\alpha(\alpha', t)\, d\alpha'/2\pi. \tag{3.6}$$

Thus, given $\hat{x}(\alpha, t)$, $\hat{y}(\alpha, t)$ for any t, we may determine $u(\alpha)$ and y_∞ (also dependent on t) by interspersed Gaussian quadrature and the Newton–Raphson method, as detailed in [5].

With $u(\alpha)$ in hand, the entire conformal map can be obtained by applying Eqs. (3.4a) and (3.4b) to the same $\bar{f}(w)$. The resulting singular integrals can be

2. *The Velocity Potential and Velocity Components*

The velocity potential $\phi(x, y, t)$ and the associated stream function $\psi(x, y, t)$ together form an analytic (and periodic) function

$$\Phi(z) = \phi(x, y, t) + i\psi(x, y, t)$$

and this can be referred to the w plane via

$$\bar{\Phi}(w) = \Phi(z(w)).$$

Then $d\Phi/dz$ and $d\bar{\Phi}/dw$ are analytic and periodic as well and can be referred either to the w plane for the purposes of calculation or to the z-plane for interpretation. The x and y components of fluid velocity are expressed by

$$\frac{d\Phi}{dz} = \phi_x(x, y, t) - i\phi_y(x, y, t).$$

The normal and tangential velocities on the boundary are given by

$$\left(\frac{d\bar{\Phi}}{dw}\right)_{u=u(\alpha), v=0} = \left(\frac{\partial\phi}{\partial u} - i\frac{\partial\phi}{\partial v}\right)_{u=u(\alpha), v=0} = |F_s(\alpha, t) - iF_n(\alpha, t)|\, ds/du,$$

where $s = s(\alpha)$ represents arc length on the interface and

$$ds/du = s_\alpha(\alpha)/u_\alpha(\alpha) = |\hat{x}_\alpha(\alpha, t)^2 + \hat{y}_\alpha(\alpha, t)^2|^{1/2}/u_\alpha(\alpha).$$

Applying Eqs. (3.4a) and (3.4b) to $d\bar{\Phi}/dw$ on the interface, with a subtraction based on Eq. (3.2a), we have

$$F_\alpha(\alpha) = s_\alpha(\alpha)\, F_s(\alpha) = -\int_{-\pi}^{\pi} G_u(u(\alpha), u(\alpha'))$$
$$\times |u_\alpha(\alpha)\, s_\alpha(\alpha')\, F_n(\alpha') - u_\alpha(\alpha')\, s_\alpha(\alpha)\, F_n(\alpha)|\, d\alpha'/2\pi, \tag{3.8a}$$

$$s_\alpha(\alpha)\, F_n(\alpha) = \int_{-\pi}^{\pi} G_u(u(\alpha), u(\alpha'))|u_\alpha(\alpha)\, F_\alpha(\alpha') - u_\alpha(\alpha')\, F_\alpha(\alpha)|\, d\alpha'/2\pi. \tag{3.8b}$$

Equation (3.8a) is the explicit representation of Eq. (2.13) for the upper fluid and Eq. (3.8b) is the inverse relation. For the lower fluid, we would use Green's function and map for the lower half plane.

The potential, stream function, and velocity components ϕ_x, ϕ_y can be found from their boundary values by applying Eqs. (3.4a) and (3.4b) to $\Phi(z)$ and $d\Phi(z)/dz$, again with appropriate subtractions to regularize the integrals.

3. *The Pressure*

Consider $\partial\Phi(z)/\partial t = \phi_t + i\psi_t$, whose real part is related to pressure by Eq. (2.7). Once the system of interface equations is solved, F_n is known as a function of t, and

F can be found by means of Eq. (3.3). Numerical differentiation with respect to t yields F_t and hence ϕ_t on the interface. Our prescriptions then define ψ_t on the interface. Then ϕ_t and hence P are determined in the interior from ψ_t, after the velocity components and $|\nabla\phi|^2$ have been determined.

Alternatively, ϕ_t in the interior could be obtained directly from ϕ_t on the boundary by an analytic continuation of Eq. (3.4b), i.e., by extending $G(w, w')$ to the complex Green's function. But this representation would have a nearly singular kernel for interior points close to the boundary; a numerical quadrature would likely have lower relative accuracy than in the approach we have detailed.

IV. Numerical Methods

A. *Equations for Single Fluid*

The single fluid problem is the limiting case in which the density of the lower fluid $\bar{\rho} \to 0$. The interface becomes a free surface on which the pressure is a constant. It simplifies both the physics and the mathematics and represents the physical limit in which the kinetic energy of the lower fluid is small compared to that of the upper fluid.

In this case the equations for the motion of the boundary are

$$\mathbf{n} \cdot (\hat{x}_t, \hat{y}_t) = F_n, \tag{4.1}$$

$$\mathbf{s} \cdot (\hat{x}_t, \hat{y}_t) = v_s, \tag{4.2}$$

$$F_t = \tfrac{1}{2}F_n^2 + F_s(v_s - \tfrac{1}{2}F_s) - g\hat{y} - \sigma(\rho R)^{-1}. \tag{4.3}$$

A time varying function independent of x and y has been absorbed into the potential to eliminate the pressure from the last equation. This is possible since the pressure is constant on the interface.

As a further simplification we consider the case in which the interface and potential are even-periodic with wavelength 2π,

$$\phi(x, y) = \phi(x + 2\pi, y) = \phi(-x, y). \tag{4.4}$$

In this case we need only consider a half wavelength $0 \leqslant x \leqslant \pi$. The boundary function of the conformal map satisfies the equation [5]

To compute the value of an analytic function in the interior of the fluid from the value of the real part on the interface we use the formulas

$$f_I(w) = -\mathrm{Re}\left[\sin w \int_0^\pi \frac{f_R(u(\alpha)) - f_R(u)}{\cos w - \cos u(\alpha)} u_\alpha(\alpha)\, d\alpha/\pi\right], \tag{4.7a}$$

$$f_R(w) = f_R(\infty) + \mathrm{Re}\left[\int_0^\pi \frac{f_I(u(\alpha)) \sin u(\alpha) - f_I(u) \sin u}{\cos w - \cos u(\alpha)} u_\alpha(\alpha)\, d\alpha/\pi\right]. \tag{4.7b}$$

These integrals have been regularized by subtractions for efficient evaluation by numerical quadrature.

B. *Differencing Scheme*

The differencing scheme we used to solve Eqs. (4.1)–(4.6) numerically was guided by the need to evaluate integrals by quadrature. The integrals in Eqs. (4.5) and (4.6) have been regularized to be nonsingular. However, the integrand at $\alpha' = \alpha$ is formally 0/0. Its value at this point is determined by continuity. Rather than computing this by interpolation or L'Hopital's rule we evaluate the integrals by an interspersed quadrature scheme described in Ref. 5. To do this, the variable α which parameterizes the interface is discretized at the nodes of a pair of interspersed quadrature rules. For example, to exploit the periodicity, we may use the Gauss and Lobatto-Chebyshev quadrature by choosing the $2N + 1$ points

$$\alpha_i = (i - 1)\pi/(2N) \qquad \text{for} \quad i = 1, 2, \ldots, 2N + 1. \tag{4.8}$$

Then we introduce the variables

$$x_i(t) = \hat{x}(\alpha_i, t), \qquad y_i(t) = \hat{y}(\alpha_i, t), \qquad \text{and} \qquad F_i(t) = F(\alpha_i, t). \tag{4.9}$$

For a Gauss point (α_i with i even) we evaluate the integrals using the Lobatto points as nodes,

$$\int_0^\pi f(\alpha_i, \alpha')\, d\alpha'/\pi = (1/N) \sum_{j\,\mathrm{odd}} \varepsilon_j f(\alpha_i, \alpha_j),$$

where $\varepsilon_1 = \varepsilon_{2N+1} = \frac{1}{2}$ and $\varepsilon_j = 1$ otherwise; and for a Lobatto point (α_i with i odd)

If we equate the Gauss and the Lobatto quadratures of

$$\int_0^\pi \frac{f(\alpha)-f(\alpha')}{\cos\alpha-\cos\alpha'}\frac{d\alpha'}{\pi},$$

we have

$$\sum_{i\,\text{odd}} \varepsilon_i \frac{f(\alpha)-f(\alpha_i)}{\cos\alpha-\cos\alpha_i} = \sum_{i\,\text{even}} \frac{f(\alpha)-f(\alpha_i)}{\cos\alpha-\cos\alpha_i}.$$

Then as α approaches one of the α_i, this equations defines $(df/d\alpha)_{\alpha=\alpha_i}$ in terms of the $2N+1$ $f(\alpha)$ values on the mesh. The global derivative, so defined, is exact if $f(\alpha)$ is a polynomial in $\cos\alpha$ of degree not exceeding $2N$, the level of accuracy consistent with the quadrature formulas. This approach was very successful for the early stages of the Rayleigh–Taylor development and for a number of other test problems. It became unreliable for the calculation of $du/d\alpha$ as the spike became sharp ($t \gtrsim 3$ in the examples of the next section), apparently because the near-singular behavior of u near $x=0$ made the calculation of $du/d\alpha$ unstable near $x=\pi$. That is, the "global" high-order nature of the method becomes a disadvantage at this point.

Lacking a suitable fix for this difficulty, we then approximated $du/d\alpha$ by an n-point Lagrangian difference formula. This discretization results in a system of $3(2N+1)$ ordinary differential equations for $x_i(t)$, $y_i(t)$, and $F_i(t)$. These are then integrated in time quite efficiently using the routine ODE. This uses a variable time step and variable order Adam's method and is described in detail in [6].

C. *Parameterization of the Interface*

Two parameterizations of the interface were used. The first corresponds to an Eulerian method with a fixed grid along the x axis. This is accomplished by choosing

$$v_s = -n_y F_n, \tag{4.10}$$

where n_y is the y component of the unit normal, in order that $\hat{x}_t = 0$. Thus, we may take $\alpha \equiv x$ and eliminate one set of equations. The motion of the surface is described by

$$\hat{y}_t(x,t) = F_n(x,t)[1+\hat{y}_x^2]^{1/2}. \tag{4.11}$$

This simplification is possible in principle when the interface $\hat{y}(x)$ is single valued. In the Rayleigh–Taylor problem, as time progresses, the spike gets very narrow and, in practice, grid resolution becomes insufficient to follow it.

The second parameterization corresponds to a Lagrangian method in which the grid points move with the fluid. This is accomplished by choosing $v_s = F_s$. For the Rayleigh–Taylor problem it has the advantage of concentrating the grid points in the region where the slope of the interface is steepest. It also increases the resolution in the spike region but decreases the resolution in the bubble region.

The parameterization has an important effect on the numerical instability. This is discussed in Section E.

D. *Diagnostics*

Two quantities, the flux and the energy, are useful as diagnostics to indicate the quality of the calculation. For an incompressible fluid the flux must vanish.

$$\text{flux} = \int_0^\pi F_n s_\alpha \, d\alpha = 0. \tag{4.12}$$

Numerical calculations of (4.12) provide a check on the solution of the potential problem and the adequacy of the mesh as a function of time.

The total energy E is a conserved quantity. It is the sum of three terms:

$$\text{Potential energy} = -\frac{1}{2}\int_0^\pi \hat{y}^2 \hat{x}_\alpha \, d\alpha, \tag{4.13a}$$

$$\text{Kinetic energy} = \frac{1}{2}\int_0^\pi d\alpha \, \hat{x}_\alpha \int_{\hat{y}}^\infty dy \, |\nabla\phi|^2 = -\frac{1}{2}\int_0^\pi F F_n s_\alpha \, d\alpha, \tag{4.13b}$$

$$\text{Surface energy} = \sigma \int_0^\pi (s_\alpha - 1) \, d\alpha. \tag{4.13c}$$

The potential and surface energy are relative to the unperturbed surface $\hat{y} = 0$. Note, an additive constant to the potential does not effect the kinetic energy because the flux vanishes. The relative change in energy over time,

$$(E(t) - E(0))/E(0),$$

should be zero, and its deviation from zero in the calculation provides a check on the accumulation of errors from the time integration.

The flux and relative error in the energy are average quantities. They are not sufficient to determine the accuracy of the calculation but seem to be good indicators of it. An additional indicator is the smoothness of the solution. The radius of curvature is a sensitive quantity for this purpose.

E. *Numerical Stability*

The calculation of the fluid flow for the Rayleigh–Taylor instability problem is sensitive to numerical errors. These errors introduce perturbations with half-wavelength on the order of the grid spacing. Linear theory predicts in the absence of viscosity and surface tension that the growth rate of the instability increases as the wavelength decreases. Thus, as time evolves, the growth of perturbations due to numerical errors can dominate the problem. In addition, when the problem is

discretized, the rapid elongation and narrowing of the spike leads to inaccuracies due to lack of resolution.

We have found the calculation to be quite sensitive to the parameterization scheme chosen to represent the interface. With the Eulerian grid, the typical calculation runs well up to a certain time and then rapidly breaks down as indicated by the energy diagnostic. At this point the distortion of the interface is still well within the computational capability of the conformal map scheme [5]. A symptom of the numerical breakdown is a lack of smoothness in the bubble region which leads to oscillations in the radius of curvature. A likely cause for this was having too few points to resolve the rapid variation of $\hat{y}$ and F in the transition regions between the bubble and spike. This leads to inaccuracies in evaluating the integral for F_n. The interspersed quadrature rules have errors of opposite sign and may be a contributing factor to the short wavelength oscillations. Even increasing the resolution by doubling the number of mesh points did not significantly prolong the time for which the calculation maintained accuracy.

On the other hand, with the Lagrangian grid, the calculation is numerically stable for a substantially longer time interval. The grid points tend to concentrate on the interface where the slope is steepest, improving the accuracy in evaluating the integral for F_n. In addition, the spreading apart of the grid points in the bubble region may have a stabilizing effect. This increases the wavelength of the numerical disturbances and thus decreases their growth rate. A similar effect for vortices was pointed out in [7].

A related question is whether the flow in the nonlinear regime is stable to small perturbations. The examples in the next section indicate that the flow for a single fluid asymptotically approaches a steady state consisting of a rising bubble and a falling spike. In the linear theory the instability is driven by the effective gravity $g - a(t)$. In the nonlinear regime the fluid acceleration is close to 0 at the tip of the bubble and increases to exceed gravity slightly in the spike region. This suggests the spike region is locally stable. The bubble region may be locally stable due to the tangential velocity neglected in the linear theory which stretches the wavelength and flows disturbances towards the spike. The transition region between the bubble and spike may be stabilized by a combination of the tangential flow stretching the arc length and the slope of the interface which decreases the component of the effective acceleration normal to the interface. Thus, the nonlinear flow may be physically stable to small perturbations and can be well behaved numerically. This is special for a single fluid due to the absence of a subsequent Kelvin–Helmholtz instability (growth rate proportional to the product of the densities of the two fluids).

The calculation is also sensitive to the method of computing derivatives, especially of u_α. We first applied the method in [5] to calculate u_α by evaluating the integral in Eq. (4.5) by both quadrature rules and applying L'Hôpital's rule at the point $\alpha = \alpha'$. With the Eulerian grid, due to a fortuitous choice of points, the flux is negligibly small. With the Lagrangian grid, the flux diagnostic breaks down as the amplitude of the interface increases. This is the result of an incompatibility between the derivative scheme and the quadrature rule. This shows up in errors in computing the integral

$\int_0^\pi u_\alpha(\alpha)\,d\alpha = \pi$. However, the quadrature rule does evaluate the integral exactly when u_α is computed by a Lagrangian rule. As the amplitude of the interface increases, u_α varies over as many as 10 orders of magnitude in our example. With a Lagrangian grid, there are a sufficient number of points for each e-folding of u_α for the Lagrangian rule to give accurate results for the derivative. This is not the case for the Eulerian grid and was the motivation for the derivative scheme developed in [5].

Finally, the time integration has to be sufficiently accurate to avoid inaccuracies due to roundoff errors in computing the derivatives. The Lagrangian calculation breaks down due to either loss of resolution in the spike region or roundoff errors.

F. *Computer Time*

The principal tasks which determined the computer time were the integrating of the dynamical equation and determining the conformal map at each time step. We took two approaches to the conformal map.

The first involved a Newton–Raphson iteration as prescribed in [5]. The map at the previous time step provides a good initial guess and typically only three iterations are needed. Each iteration involves a matrix inversion and this uses the larger portion of the computer time. Alternatively, an analytic expression for the needed matrix inverse is provided by the formula derived in [5]

$$\delta u(x) = \sin u(x) \int_0^\pi \frac{u_x(x')^2}{1 + \hat{y}_x(x')^2} \frac{\delta\hat{y}(x) - \delta\hat{y}(x')}{\cos u(x) - \cos u(x')}\,dx'/\pi. \tag{4.14}$$

For large meshes, computing time for obtaining the conformal map by this route is proportional to N^2, rather than N^3 for the Newton–Raphson. Therefore, this approach might well be preferable for application of complex variable to more benign flow problems. It proved less reliable for the Rayleigh–Taylor problem, however, and required significantly more iterations (convergence is linear rather than quadratic).

Even so, the calculation is very fast. With $2N + 1 = 41$ points, to go from a peak to peak amplitude of 1 to 5.7 (example in Section V.B up to $t = 3$) took 15 seconds on the CDC 7600. As the amplitude increases the time step decreases and the computer time increases. The calculations described in the next section used 81 points. The longest required less than three minutes on the CDC 7600.

G. *Variables in the Interior*

Because the map variables and all fluid variables of interest are components of analytic functions, Eqs. (3.4a) and (3.4b) determine their interior values in terms of boundary data. This approach, utilizing interspersed Gauss quadrature and suitable regularization, worked well in our numerical experiments.

We note here an alternative approach with advantages of its own, namely the method of analytic modeling. A set of parameters is found from the numerical boundary data and the functions whose interior values are sought are then represented

as explicit analytic functions depending on the parameters. The fluid variables are modeled in the w plane and referred to the physical plane via a modeling of the conformal map.

For a periodic function $f(w)$, analytic in the upper half plane, we might attempt a Fourier series modeling

$$f(w) = f_\infty + \sum_{n=1}^{N} a_n e^{inw}.$$

But, as we shall show elsewhere, the number N of Fourier terms needed for merely order-of-magnitude accuracy near the trough of a boundary can be estimated by

$$N \gtrsim \tfrac{1}{2}(u_x)^{-1}.$$

Now the u_x values dealt with in this paper range down to 10^{-11} and are characteristically less than 10^{-3} for Rayleigh–Taylor flows well into the nonlinear regime. Thus, Fourier series modeling is unworkable for most of the phenomena addressed in this paper.

A model which does work well is the following partial fractions representation:

$$f(w) = f_\infty - \sum_{n=1}^{N} \varepsilon_n \frac{2e^{iw}}{e^{\alpha_n} - e^{iw}}.$$

For our present purposes, we assume that the parameters f_∞, ε_n, α_n are real so that $f(w)$ is even-periodic. (The treatment is easily generalized.) Then on the real line,

$$f_R(u) = f_\infty + \sum_{n=1}^{N} \varepsilon_n \frac{\sinh \alpha_n}{\cosh \alpha_n - \cos u} - 1,$$

$$f_I(u) = \sum_{n=1}^{N} \varepsilon_n \left\{ \frac{\sin u}{\cosh \alpha_n - \cos u} \right\}.$$

A sum over N fractions requires $2N + 1$ parameters, including f_∞. Given, say, $2N + 1$ data points for $f_R(u)$, we may (a) express $f_R(u)$ as a simple continued fraction in the variable $\cos u$, or better, in $1 - \cos u$, using the Thiele algorithm [8] and (b) re-express the continued fraction as a ratio of polynomials, then resolve it into partial

Then P is obtained from $f(w)$ and a previous calculation of the velocity field, while $f(w)$ itself is determined from the boundary values $f_R(u) = F_t$.

Figures 10–14, described in Section V, were obtained by this method.

V. Illustrative Numerical Results

A principal interest of these numerical calculations is to study the large amplitude nonlinear effects on Rayleigh–Taylor instability. We begin with the case of a small amplitude perturbation, both as a check on the calculations and to determine when the linear theory breaks down. With an initial perturbation on the surface displacement $\hat{y} = A_0 \cos(kx)$ and $\underline{v} = 0$ the linear theory [2] predicts exponential growth,

$$\hat{y} = A_0 \cos(\alpha t) \cos(kx), \tag{5.1}$$

where

$$\alpha = \{|kg(\rho - \bar{\rho}) - \sigma k^3|/(\rho + \bar{\rho})\}^{1/2} \tag{5.2}$$

is the growth rate and $k = 2\pi/\lambda$ is the wavenumber, for wavelengths

$$\lambda > \lambda_c = 2\pi|\sigma/(\rho - \bar{\rho})g|^{1/2}. \tag{5.3}$$

It is convenient to choose the units of length and time such that the wavelength of the perturbation is $\lambda = 2\pi(k = 1)$ and the gravitational acceleration is $g = 1$. This is equivalent to scaling to dimensionless variables $\tilde{x} = kx$ and $\tilde{t} = (kg)^{1/2}t$. For zero surface tension $\sigma = 0$, the motion depends only on the Atwood ratio $(\rho - \bar{\rho})/(\rho + \bar{\rho})$ since both the gravitational force and inertial mass scale with density. The following calculations are for a single fluid ($\bar{\rho} = 0$) and were performed on Lagrangian grids with up to 81 points.

A. *Small Amplitude Perturbation* ($kA_0 = 0.01$)

In the first calculation we consider a small amplitude perturbation

$$\hat{y} = -0.01 \cos x \qquad \text{and} \qquad \mathbf{v} = 0.$$

The time evolution of the interface along with the trajectories of interface points is shown in Fig. 1. Nonlinear effects distort the shape of the interface into a rising bubble ($x = \pi$) and falling spike ($x = 0$). In the spike region, the trajectories are approaching vertical indicating that the particles are falling with gravity. In order to conserve mass, the trajectories in the bubble rise and are swept towards the spike.

To compare with the linear theory, the log amplitude A versus time is plotted in Fig. 2 for the tip of the bubble and the tip of the spike. At early times the amplitudes of the bubble and spike agree with the linear theory. Subsequently, the amplitude of

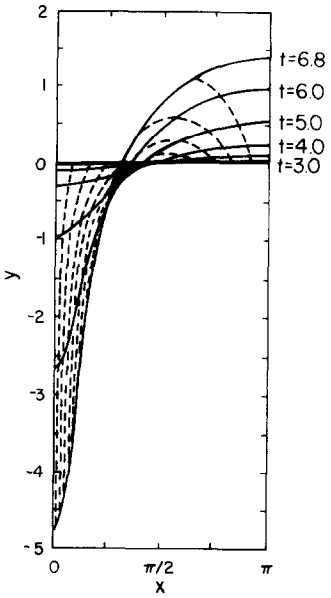

FIG. 1. The time evolution of the interface and trajectory of points on the interface starting from a small amplitude perturbation $\hat{y} = -0.01 \cos x$ and $\mathbf{v} = 0$ at $t = 0$.

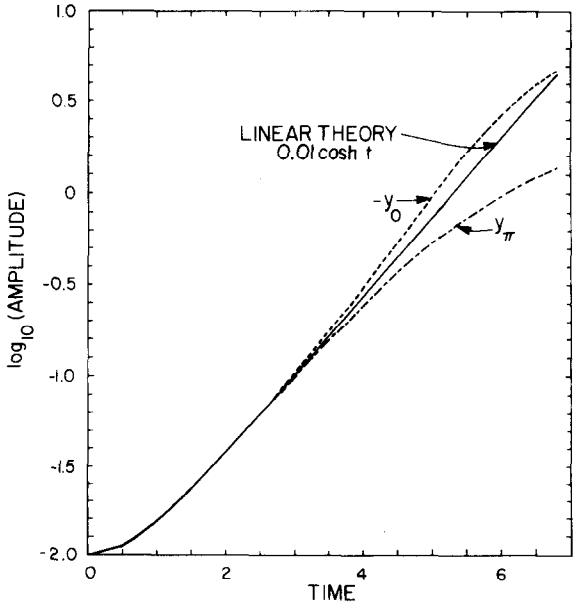

FIG. 2. Comparison with linear theory. Log (amplitude) versus time for the tip of the bubble and the tip of the spike for an initial perturbation $\hat{y} = -0.01 \cos x$ and $\mathbf{v} = 0$ at $t = 0$.

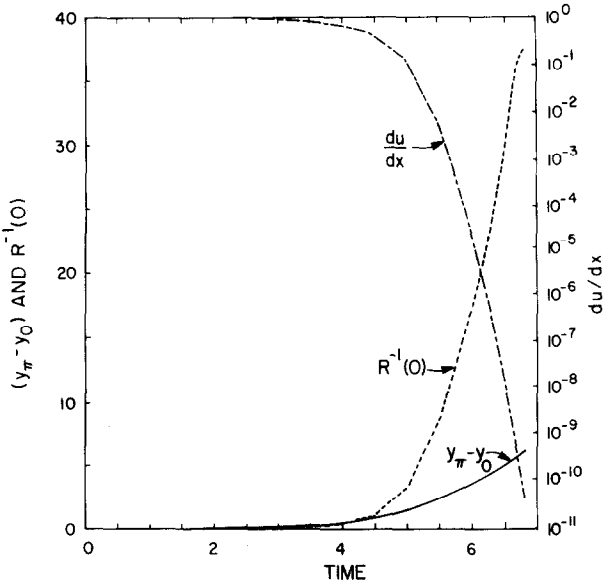

FIG. 3. Peak to peak amplitude, curvature at the tip of the spike and crowding of the conformal map versus time for an initial perturbation $\hat{y} = -0.01 \cos x$ and $\mathbf{v} = 0$ at $t = 0$.

the spike is larger and the amplitude of the bubble is smaller than the linear theory. Later, the linear theory amplitudes will be higher in both the bubble and the spike since asymptotically

$$\begin{aligned} \log A &\to t, && \text{for the linear theory,} \\ &\to 2 \log t, && \text{for the tip of the spike,} \\ &\to \log t, && \text{for the tip of the bubble.} \end{aligned}$$

The deviation from the linear theory becomes significant at about $kA \approx 1$.

The computational difficulty in this problem arises from solving the potential problem in progressively more highly distorted regions resulting from the elongation and narrowing of the spike. This results in severe crowding of the conformal map. The peak-to-peak amplitude, the curvature at the tip of the spike and $\log(u_x)$ at the tip of the spike, which is a measure of the crowding of the conformal map, are shown in Fig. 3. The diagnostics indicate the calculation breaks down at a time when $u_x \sim 5 \times 10^{-11}$; before this time the accuracy decreases slowly and afterwards degenerates rapidly.

B. *Large Amplitude Perturbation* ($kA_0 = 0.5$)

To get further into the asymptotic region we consider an initial large amplitude perturbation $\hat{y} = -0.5 \cos x$ and $\mathbf{v} = 0$. Figure 4 shows the time evolution of the shape

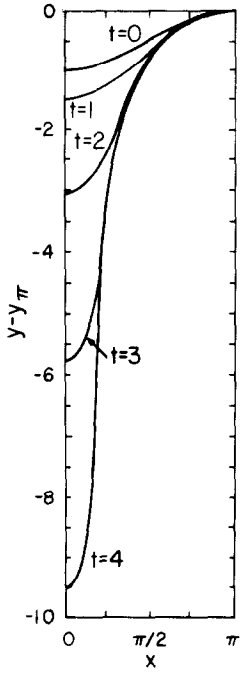

FIG. 4. The time evolution of the shape of the interface normalized to the tip of the bubble for an initial perturbation $\hat{y} = -0.5 \cos x$ and $\mathbf{v} = 0$ at $t = 0$.

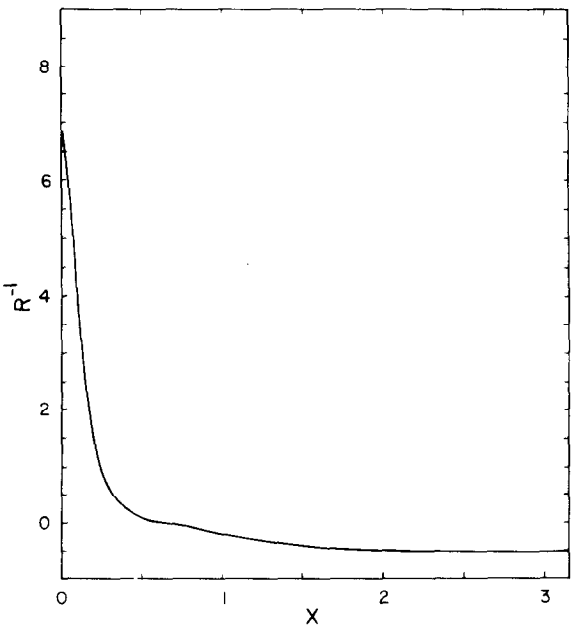

FIG. 5. Curvature versus x at $t = 3.75$ for an initial perturbation $\hat{y} = -0.5 \cos x$ and $\mathbf{v} = 0$ at $t = 0$.

of the interface by plotting it relative to the tip of the bubble. As time evolves it appears as if the interface is tracking out a larger and larger portion of an asymptotic steady state shape. The curvature is plotted in Fig. 5. The curvation is approximately constant in the bubble region and $R^{-1} = 0.51\,\mathrm{k}$ at the tip. Thus the bubble approaches a nearly circular shape. This was observed experimentally by Davies and Taylor [9].

In Fig. 6, the time development of the velocity of the bubble and the acceleration of the tip of the spike are shown. The bubble approaches a constant velocity $v_b = 0.23(\lambda g)^{1/2}$. The acceleration of the spike overshoots free fall. The overshoot in the acceleration is due to a contribution from the gradient of the pressure. The flow from the bubble to the spike on each side of the symmetry line above the tip of the spike is similar to two streams of fluid colliding. A peak pressure develops on the line of symmetry giving rise to a pressure gradient which decelerates the horizontal particle velocity and also accelerates the vertical particle velocity. We believe the R^{-1} and v_b calculations are accurate to at least the two figures shown.

Figure 7 shows the potential versus the vertical displacement on the interface. A constant has been added to the potential in order that it vanish at infinity (i.e., $\phi_\infty = \int_0^\pi F(x)\, u_x dx/\pi = 0$) and the vertical displacement is measured relative to the tip of the bubble. With this normalization a longer and longer portion of an asymptotic

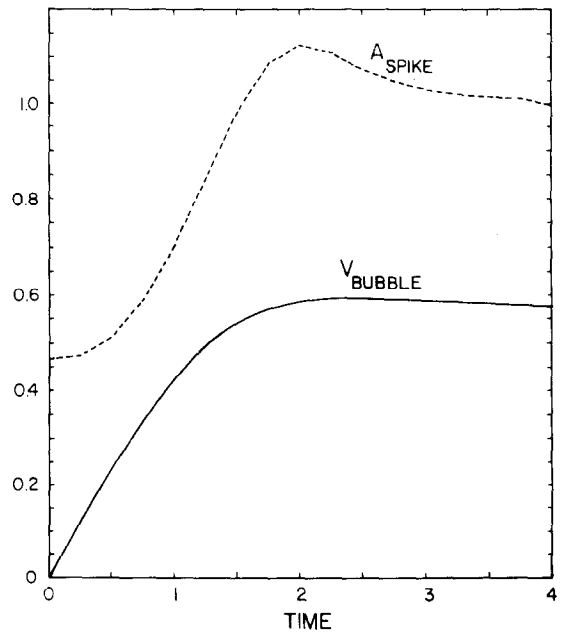

FIG. 6. The time development of the velocity of the tip of the bubble and acceleration of the tip of the spike for an initial perturbation $\hat{y} = -0.5 \cos x$ and $\mathbf{v} = 0$ at $t = 0$.

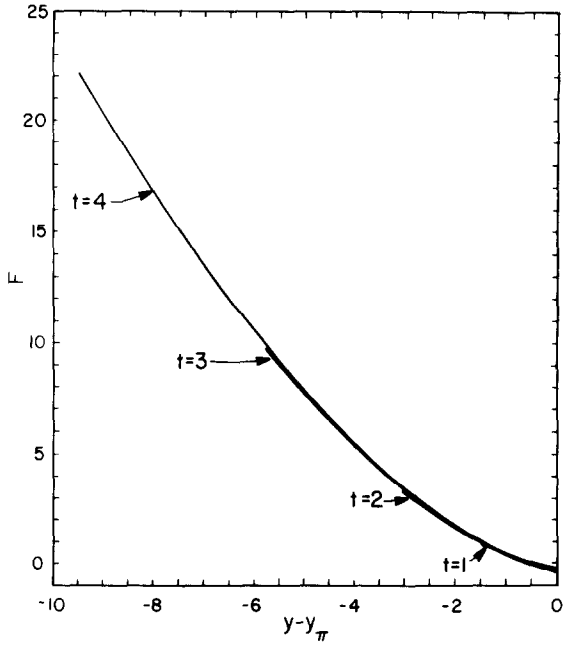

FIG. 7. The potential versus vertical displacement on the interface for an initial perturbation $\hat{y} = -0.5 \cos x$ and $\mathbf{v} = 0$ at $t = 0$.

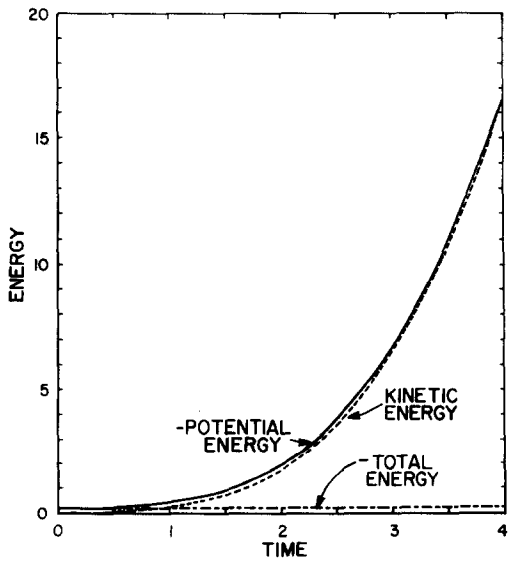

FIG. 8. Energy versus time for an initial perturbation $\hat{y} = -0.5 \cos x$ and $\mathbf{v} = 0$ at $t = 0$.

steady state curve $[F \to (\frac{8}{9})^{1/2}(-y)^{3/2}$ as $y \to -\infty]$ is being traced out in time. This implies the potential in the interior of the fluid is approaching a steady state in the frame of reference rising with the bubble, i.e., $(d/dt)\,\phi(x, y - v_{\text{bubble}}t, t) \to 0$. In the Appendix, the properties of the steady state solution are derived.

Figure 8 shows the energy versus time. Asymptotically the kinetic energy (and hence the potential energy) is expected to vary as t^3 since the effective mass increases linearly (constant velocity of the bubble) and the effective velocity increases linearly (free fall of the spike). The diagnostic of the total energy is seen to remain constant to a high accuracy for the time interval depicted.

The crowding in the conformal map is shown in the plot of $\log(u_x)$ versus x in Fig. 9. In the bubble region, the boundary map function is approximately constant. This is the result of the bubble approaching a constant shape and the spike region having a small effect on the map in the bubble region (which follows from Eq. (4.14)). This calculation breaks down due to loss of resolution in the spike when $u_x(0) = 3 \times 10^{-10}$.

We have computed the flow in the interior of the fluid from the potential on the boundary at $t = 3$. Figure 10 shows the image in the z plane under the conformal map of a rectangular grid in the w plane. In the spike region the mesh is highly crowded. Above the tip of the bubble a rectangular grid is rapidly approached. Figure 11 is a

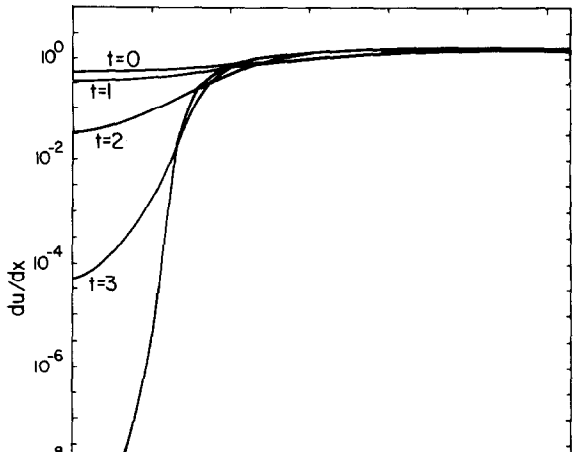

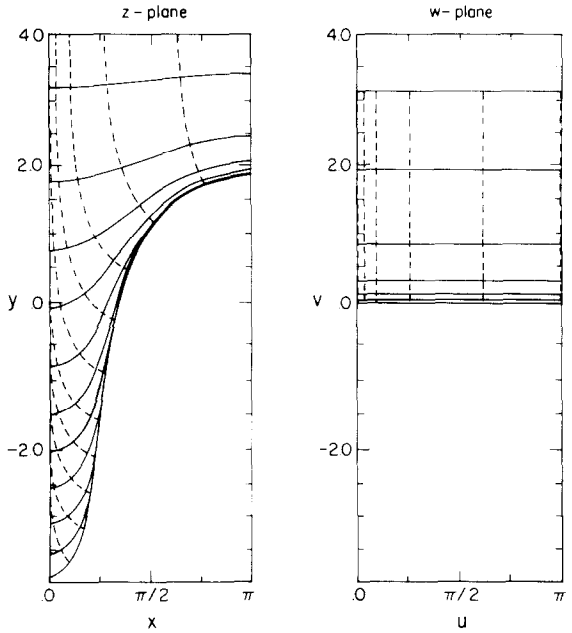

FIG. 10. Image in the z plane of the conformal map of rectangular grid in the w plane at $t = 3$ for an initial perturbation $\hat{y} = -0.5 \cos x$ and $\mathbf{v} = 0$ at $t = 0$.

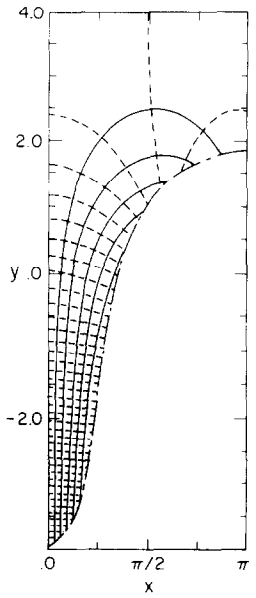

FIG. 11. Contour plot of potential (dotted) and stream function (solid) at $t = 3$ for an initial perturbation $\hat{y} = -0.5 \cos x$ and $\mathbf{v} = 0$ at $t = 0$. The range of the potential contours is from -0.5 to 9.5 in steps of 0.25. The range of the stream function contours is from 0 to 1.5 in steps of 0.25.

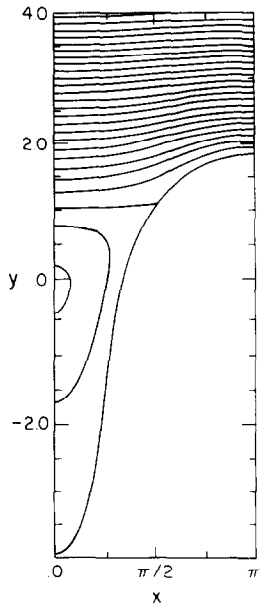

FIG. 12. Contour plot of pressure at $t = 3$ for an initial perturbation $\hat{y} = -0.5 \cos x$ and $\mathbf{v} = 0$ at $t = 0$. The pressure is taken as zero on the interface. It ranges from slightly above 0.2 near the origin down to -2.3 at the top of the graph ($y = 4$), with contours shown in steps of 0.1.

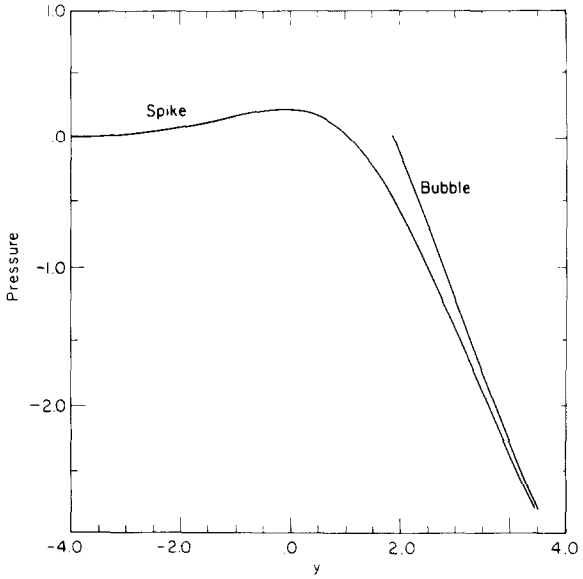

contour plot of the potential and stream function. The streamlines from the fluid rise above the bubble and are swept down the spike. The streamlines in the spike region approach vertical lines indicating the fluid is tending towards free fall. Figure 12 is a contour plot of P. The pressure has a peak above the spike. Figure 13 is a one-dimensional plot of P versus y above the tip of the spike and the bubble. It shows that the pressure rapidly approaches its equilibrium value $(-gy)$ above the tip of the bubble. Figure 14 is a plot of the vertical velocity versus y above the tip of the spike and above the tip of the bubble. It shows the rapid decrease in velocity, $v \sim \exp(-ky)$, above the tip of the bubble.

Figures 10–14 were obtained by the analytic modeling from the boundary values of $z(w)$, Φ, $d\Phi/dz$, and $\partial\Phi/\partial t$, according to the partial fractions representation prescribed in section IV.G. To indicate the character of the modeling, we list in Table I the parameters, f_∞, ε_n, a_n, $1 \leqslant n \leqslant 10$, for the representation of each of these four functions obtained by a 21-point fit to the calculated values of their real parts on the interface. The interior values may be obtained to at least the accuracy of the boundary values, but the quoted three-figure accuracy is sufficient for the graphs.

C. *Velocity Perturbations* $[v_0 = 0.5(g/k)^{1/2}]$

Due to the nonlinearities, the approach to the steady state depends on the initial perturbation resulting from the potential $\phi(x, y) = 0.5\cos(x)\exp(-y)$ and an unperturbed interface $\hat{y} = 0$.

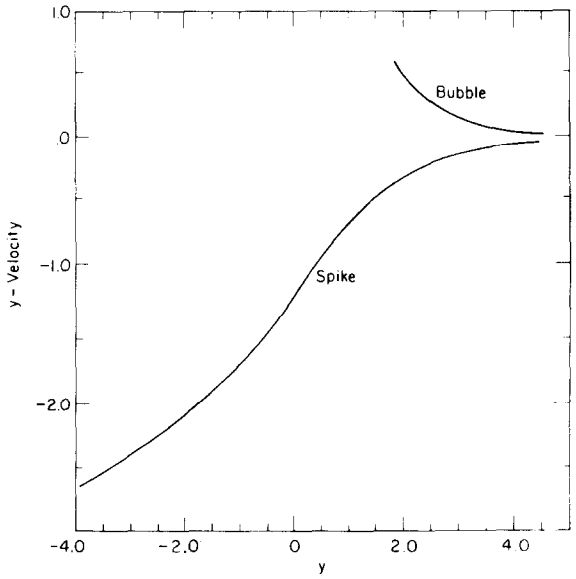

FIG. 14. Velocity versus distance above the tip of the bubble and the tip of the spike at $t = 3$ for an initial perturbation $\hat{y} = -0.5\cos x$ and $\mathbf{v} = 0$ at $t = 0$.

TABLE I

Parameters for the analytic modeling by partial fractions of the four analytic functions which determine the fluid variables in the interior of the fluid

	$z(w)$		Φ		$d\Phi/dz$		$\partial\Phi/\partial t$	
n	ε_n	α_n	ε_n	α_n	ε_n	α_n	ε_n	α_n
1	-1.93×10^{-6}	1.79×10^{-5}	5.13×10^{-6}	1.47×10^{-5}	-4.20×10^{-7}	1.83×10^{-4}	-8.51×10^{-7}	1.78×10^{-5}
2	-1.81×10^{-5}	8.34×10^{-5}	4.64×10^{-5}	8.25×10^{-5}	-4.47×10^{-6}	8.62×10^{-5}	-7.06×10^{-6}	8.06×10^{-5}
3	-9.53×10^{-5}	3.59×10^{-4}	2.31×10^{-4}	3.53×10^{-4}	-2.71×10^{-5}	3.71×10^{-4}	-3.22×10^{-5}	3.47×10^{-4}
4	-3.49×10^{-4}	1.33×10^{-3}	7.90×10^{-4}	1.31×10^{-3}	-1.12×10^{-4}	1.37×10^{-3}	-1.07×10^{-4}	1.31×10^{-3}
5	-1.12×10^{-3}	4.22×10^{-3}	2.33×10^{-3}	4.13×10^{-3}	-3.98×10^{-4}	4.34×10^{-3}	-3.32×10^{-4}	4.21×10^{-3}
6	-3.76×10^{-3}	1.30×10^{-2}	7.09×10^{-3}	1.26×10^{-2}	-1.51×10^{-3}	1.34×10^{-2}	-1.16×10^{-3}	1.31×10^{-2}
7	-1.41×10^{-2}	4.20×10^{-2}	2.32×10^{-2}	4.04×10^{-2}	-6.67×10^{-3}	4.41×10^{-2}	-4.86×10^{-3}	4.34×10^{-2}
8	-5.85×10^{-2}	1.48×10^{-1}	7.90×10^{-2}	1.40×10^{-1}	-3.65×10^{-2}	1.60×10^{-1}	-2.48×10^{-2}	1.56×10^{-1}
9	-2.40×10^{-1}	5.33×10^{-1}	2.48×10^{-1}	4.98×10^{-1}	-2.33×10^{-1}	5.95×10^{-1}	-1.43×10^{-1}	5.79×10^{-1}
10	-1.02	1.88	7.44×10^{-1}	1.75	-1.70		-8.89×10^{-1}	2.01
$f_\infty =$	1.33		-1.10		0		1.68	

Note. The values are for the example of Section V.B (large amplitude initial perturbation) at $t = 3$.

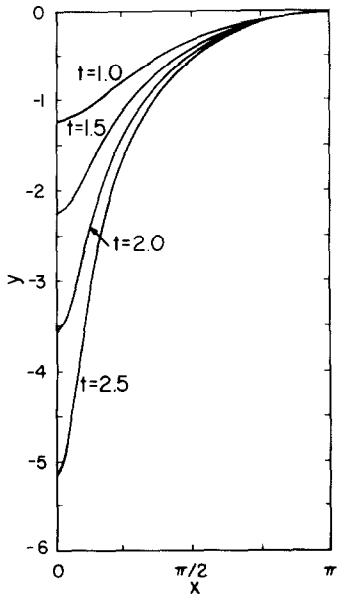

FIG. 15. The time evolution of the interface normalized to the tip of the bubble for an initial perturbation $F = -0.5 \cos x$ and $\dot{y} = 0$ at $t = 0$.

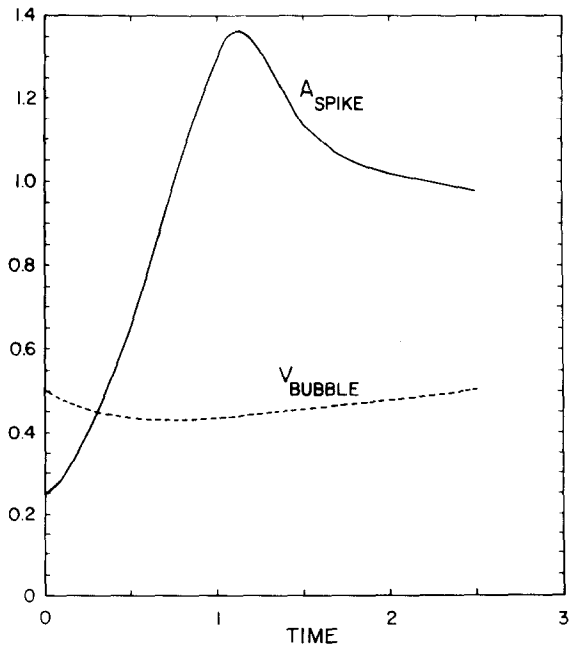

FIG. 16. The acceleration of the tip of the spike and velocity of the tip of the bubble versus time for an initial perturbation $F = 0.5 \cos x$ and $\dot{y} = 0$ at $t = 0$.

1. *With Gravity* ($g = 1$)

The time evolution of the interface is shown in Fig. 15. The interface has a similar bubble and spike shape to that in Fig. 4 for an initial surface disturbance, but the bubble is broader and the spike is narrower. As time evolves the interface is approaching the steady state shape. It appears as if the rising bubble only slowly adjusts to the wavelength imposed by the boundary conditions.

The acceleration of the spike and the velocity of the bubble are shown in Fig. 16. The acceleration of the spike overshoots the acceleration of gravity by a larger amount than in the previous case. The velocity of the bubble initially decelerates due to the pressure gradient arising from the velocity field and the condition of incompressibility. Subsequently, the bubble velocity increases towards its steady state value.

2. *Without Gravity* ($g = 0$)

A Rayleigh–Taylor type of instability can also arise when a corrugated interface is given an impulsive accelaration by a passing shock wave [10, 11]. To the extent that the compressibility of the fluid may be neglected, this case can be approximated by an initial velocity perturbation in the absence of gravity. The time scale is set by and the motion scales with the initial velocity.

The time evolution of the interface is shown in Fig. 17. If the time is adjusted appropriately, the shape of the interface is nearly the same as in the previous case

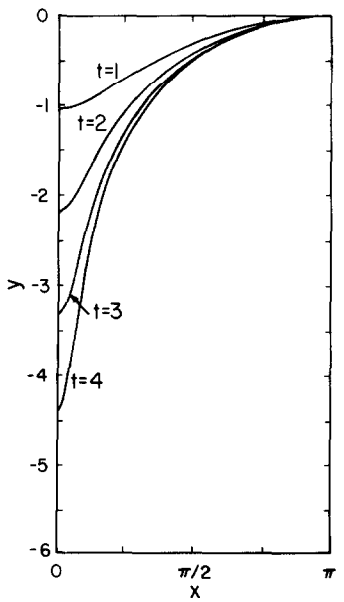

FIG. 17. The time evolution of the interface normalized to the tip of the bubble with $g = 0$ for an initial perturbation $F = 0.5 \cos x$ and $\hat{y} = 0$ at $t = 0$.

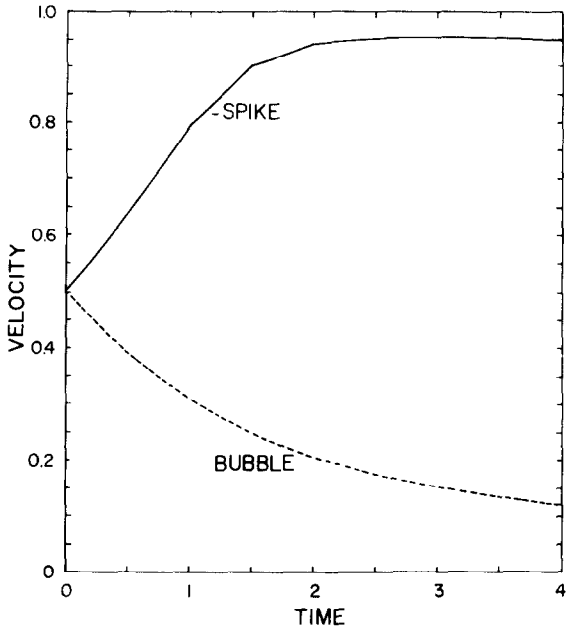

FIG. 18. The velocity of the tip of the bubble and (minus) tip of the spike versus time with $g = 0$ for an initial perturbation $F = 0.5 \cos x$ and $\hat{y} = 0$ at $t = 0$.

with gravity (Fig. 15). It appears that the main effect of gravity is to supply energy (potential energy is converted to kinetic energy) resulting in the flow occurring at a faster rate.

The velocity is shown in Fig. 18. The velocity of the spike accelerates and then levels off at about 1.8 times its initial value. The velocity of the bubble decreases towards zero. Since $P/\rho + gy + \frac{1}{2}|\nabla\phi|^2$ satisfies the Laplace equation, it follows that the initial pressure field is

$$P_0(x, y) + \rho g y = -\tfrac{1}{2}\rho F_0^2 \exp(-2y) + \text{constant} \tag{5.4}$$

for $\phi_0(x, y) = F_0^2 \cos(x) \exp(-y)$. Hence the initial particle acceleration for a point on the interface $\hat{y} = 0$ is

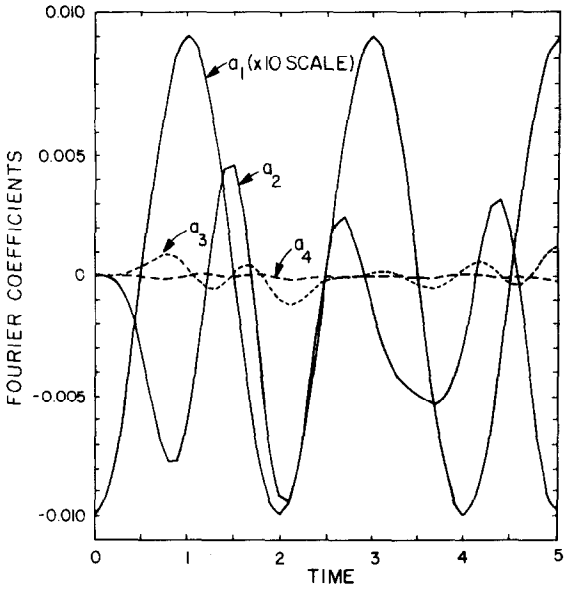

FIG. 19. Time dependence of the Fourier coefficients of the interface for the stable case with $g = -\pi^2$ and an initial perturbation $\hat{y} = -0.1 \cos x$ and $v = 0$ at $t = 0$.

D. *Stable Case*

When the sign of g is reversed, the flow becomes oscillatory (but not periodic). This is like the sloshing of a fluid in a tank (except that the fluid is on top and gravity points upward). In the following examples we choose $g = -\pi^2$ for which the linear theory predicts a period of $T = 2$. For the first case, we consider an initial small amplitude perturbation $\hat{y} = -0.1 \cos x$ and $v = 0$. The nonlinearities couple to the normal modes with shorter wavelengths and varying periods thus giving rise to aperiodic motion. This can be expressed by expanding the interface in a Fourier cosine series

$$\hat{y}(x, t) = \sum_{n=1}^{\infty} a_n(t) \cos nx.$$

The numerical calculation is very stable for this case. Figure 19 shows the first few coefficients as a function of time. The series is dominated by the first term. In this case the perturbation theory in [12] should apply.

For an initial perturbation with a larger amplitude

$$\hat{y} = -0.5 \cos x \qquad \text{and} \qquad v = 0$$

the character of the flow changes. Figure 20 shows the time development of the interface during the second half-cycle. A spike develops with larger than the initial

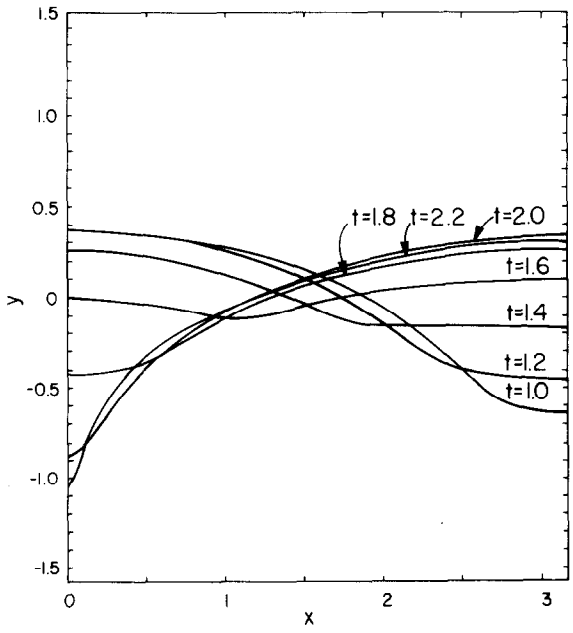

FIG. 20. Time development of the interface during the second half-cycle for the stable case $g = -\pi^2$ and an initial perturbation $\hat{y} = -0.1 \cos x$ and $\mathbf{v} = 0$ at $t = 0$.

amplitude. The calculation breaks down at $t = 2.3$ due to lack of a resolution when the curvature is $R^{-1}(0) = 123$ k. The change in the flow with increasing amplitude is undoubtedly related to the fact that with fully periodic boundary conditions traveling waves (as opposed to standing waves) only exist below a critical amplitude ($a < 0.43/\mathrm{k}$ for a single fluid) [13]. Above this amplitude breaking waves evolve because the particle velocity exceeds the phase velocity. For even-periodic conditions a similar sort of phenomenon must occur.

VI. SUMMARY

the tip of the spike overshoots and then approaches the acceleration of gravity from above. With an initial velocity perturbation, the shape of the interface with and without gravity are nearly the same if the times are selected appropriately. The main effect of gravity seems to be converting potential energy into kinetic energy resulting in the motion occurring at a faster rate. Finally, for the stable case in which the gravitational acceleration is directed into the fluid, the flow changes character above a certain amplitude. With periodic boundary conditions this method could be used to calculate surface waves.

The methods described here are directly applicable to a two-fluid Rayleigh–Taylor problem (both ρ and $\bar{\rho}$ nonzero) with two additional complications. First, for problems and for large times such that the Lagrangian grid (grid points move with the fluid) is preferable to an Eulerian grid, a 2-fluid problem requires two grids tracking the same interface, one for the variables of each fluid. Second, Eq. (2.14) cannot be inverted analytically as was the case for $\bar{\rho} = 0$, and the determination of F_n from $\tilde{F}_s$ must be done numerically, i.e., a matrix inversion after the right side of (2.14) is represented as a quadrature.

APPENDIX: Steady State Solution

The numerical results in Section V.B suggest that for one fluid with a single-frequency perturbation, the Rayleigh–Taylor flow approaches a steady state for large times. In this section, we derive the steady state relations from our general formulation and infer some general properties. This problem has previously been studied by Davies and Taylor [9], Birkhoff and Carter [14], and Garabedian [15]. We, like these authors, lack existence and uniqueness theorems; our discussion is heuristic rather than rigorously deductive.

We return to dimensional units. For even-periodic perturbations, the limiting form of the equation for the interface is taken as

$$\hat{y}(x, t) = v_b t + \text{constant} + \bar{y}(x) \tag{A.1}$$

on the basic interval $0 \leqslant kx \leqslant \pi$. Then $\bar{y}(x)$ is the envelop of the interface curves at various times represented in, say, Figs. 4, 15, and 17. We have $\bar{y}(x) \to -\infty$ as $x \to 0$ and will standardize to

offset by an infinite sink (Dirac delta-function) at $x = 0$, and consistent with the flux condition

$$\int_0^\pi F_n(x, t)(1 + \bar{y}_x(x)^2)^{1/2} \frac{d(kx)}{\pi} = 0.$$

For $x \neq 0$, (A.1) and (A.2) are also consistent with (4.11).

To complete the specification, we invoke the conformal map equations [5]. The map $z = z(w)$ that carries $0 \leqslant u \leqslant \pi$ has the general form

$$kz(w) = w + iW(e^{iw}), \tag{A.4}$$

where, for the even-periodic case, $W(\zeta)$ is a real analytic function of $\zeta = e^{iw}$ for $|\zeta| < 1$ and vanishes as $|\zeta| \to 0$, i.e., as $\operatorname{Im} w \to +\infty$. The map equations for the boundary curve and the (real) boundary potential are

$$k\bar{y}(x) = k\bar{y}_\infty + \log 2 + \int_0^\pi \log|\cos u(x) - \cos u(x')| \frac{d(kx')}{\pi} \tag{A.5}$$

and

$$F(x, t) = F_\infty(t) + \int_0^\pi \log|\cos u(x) - \cos u(x')| F_n(x', t) \times [1 - \bar{y}_x^2(x')]^{1/2} \frac{d(kx')}{\pi}. \tag{A.6}$$

Then, in the large time limit,

$$F(x, t) = F_\infty(t) + v_b(\bar{y}(x) - \bar{y}_\infty - \log 2) - (v_b/k)\log(1 - \cos u(x)). \tag{A.7}$$

Applying these ingredients to the Bernoulli equation on the boundary,

$$\frac{\partial F(x, t)}{\partial t} = \frac{1}{2}(F_n^2 - F_s^2) + \hat{y}_x F_n F_s - g\hat{y} + \text{constant},$$

with standardization (A.2), we infer

$$\frac{dF_\infty(t)}{} = -v_b t + \text{constant}$$

the boundary map function $u = u(x)$ in that limit. The determination of $u(x)$ from $y(x)$ through (A.5) together with the boundary conditions $u(0) = 0$, $u(k\pi) = \pi$ is unique. Although (A.7) is a first order differential equation for, say, $\bar{y}(x)$ in terms of $u(x)$, it has two boundary conditions, $\bar{y}(0) = -\infty$, and $\bar{y}(k\pi) = 0$ and the constant $\gamma = v_b(k/g)^{1/2}$ emerges as an (apparently unique) eigenvalue. Methods for approximate solution of this pair of equations will be discussed elsewhere.

In the spike region, i.e., near $x = 0$, $\bar{y}_x$ is large, and approach ∞ as $x \to 0$. Thus, for small x, we may neglect 1 compared to $\bar{y}_x^2$ in Eq. (A.8). The resulting equation

$$\gamma \frac{d}{d(ky)} \log(1 - \cos u(y)) = (-2by)^{1/2}$$

has the solution

$$ky = -(\tfrac{9}{8}\gamma^2)^{1/3}[\text{constant} - \log(1 - \cos u)]^{2/3}.$$

An analytic continuation of this which is consistent with (A.4) may be written as

$$kz = w - i\left(\frac{9\gamma^2}{8}\right)^{1/2}[c_0 - 2\log(1 - e^{iw})]^{2/3}, \tag{A.9}$$

where c_0 is a real constant.

More general forms consistent with (A.4) may also be written including some with additional, but weaker, essential singularities at $w = 0$. But Eq. (A.9) suffices to define the leading terms in $x(u)$ and $y(u)$ for u and hence x near zero,

$$kx(u) \approx \frac{\pi}{3}\left(\frac{9\gamma^2}{2}\right)^{1/3}(-\log u)^{-1/3}, \qquad k\bar{y}(u) \approx -\left(\frac{9\gamma^2}{2}\right)^{1/3}(-\ln u)^{2/3}.$$

Then in the limit $x \to 0$,

$$\bar{y}(x) \approx \frac{-\pi^2\gamma^2}{2k^3}\frac{1}{x^2} \tag{A.10}$$

and

$$u(x) \approx \exp\left[-\frac{\gamma^2}{6}\left(\frac{\pi}{kx}\right)^3\right]. \tag{A.11}$$

Corrections to Eq. (A.10) would include powers of x (of which the lowest, in fact, is x^4) and terms with essential singularities of the $\exp(-x^{-3})$ type.

The complex potential $\Phi(z, t)$ defined by its real part $F(x, t)$ on the boundary Eq. (A.7) is

$$\Phi(z, t) = F_\infty(t) + v_b z + \text{constant} + \Psi(z)$$

where

$$\Psi(z) = -(v_b/k)\log(\cos w(z) - 1). \tag{A.12}$$

The potential $\Psi(z)$ describes the flow in a frame moving upward with the tip of the bubble. In this frame, a uniform flow enters at $y = +\infty$ and the tip of the bubble is a stagnation point. The steady state flow and the region into which it is conformally mapped is sketched in Fig. A1. The steady state conditions imply the range of $\Psi(z)$ is the strip $-\infty < \Psi_R < \infty$, $0 < \Psi_I \leqslant \pi v_b/k$. Equation (A.12) is the conformal map onto this strip from a semi-infinite strip $0 \leqslant u \leqslant \pi$, $v \geqslant 0$. Birkhoff and Carter [14] arrived at an equation equivalent to (A.7) from this geometric equation.

Garabedian [15] claimed the flow is not unique. The question of uniqueness is related to the allowable boundary conditions at $y \to -\infty$. Adding derivatives of delta functions to the right-hand side of Eq. (A.3) would yield a variety of conditions. However, the condition of uniform flow in the spike as expressed by (A.3) appears to lead to the only physically relevant motion.

Now consider the fluid motion defined by (A.12) and (A.9) for small $|w|$, i.e., in the interior of the spike for small x and large negative y. The leading terms are

$$kz \approx -i\left(\frac{9\gamma^2}{2}\right)^{1/3}(-\log w)^{2/3}, \qquad \psi(z) \approx 2(v_b/k)(-\log w)$$

whence, to leading order,

$$\Psi(z) \approx \left(\frac{8g}{9}\right)^{1/2}(iz)^{3/2}. \tag{A.13}$$

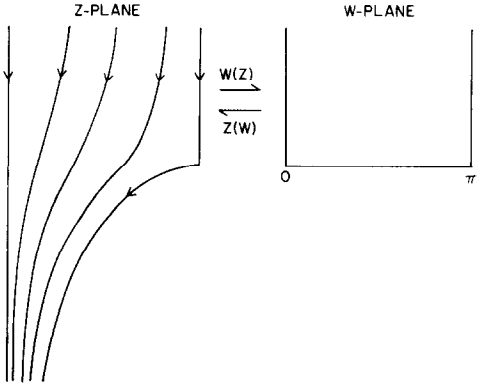

FIG. A1. Sketch of the streamlines in the z plane of the steady state flow and the region in the w plane onto which it is conformally mapped. The points $z = (0, -\infty)$ and $(\pi, 0)$ correspond to the points $w = (0, 0)$ and $(\pi, 0)$, respectively.

A complex function, which is defined in the fluid region and has the general properties of the potential, is

$$\Omega(z) = (\tfrac{8}{9})^{1/2}\{\log[A + \exp(iz)]\}^{3/2} - v_b \log[1 + B\exp(-iz)],$$

where $A > 2$ and $B > 1$. This function is analytic and even-periodic. The first term agrees with the leading term of the potential as $y \to -\infty$. The second term agrees with the leading term of the potential as $y \to +\infty$. The parameters A and B can be adjusted in order that $d\Omega/dz = 0$ at $z = \pi$, the tip of the bubble. Thus, $\Omega(z)$ provides a reasonable guess for a model of the potential.

The velocity field in the spike region from Eq. (A.13) is

$$v_x - iv_y = \frac{d\Psi(z)}{dz} \approx i(2igz)^{1/2},$$

so to first order in x,

$$v_y = -(-2gy)^{1/2}, \qquad v_x = (-x/2y)\, v_y. \tag{A.14}$$

Then the model of fluid with the spike falling in the time-independent field $\psi(z)$ at large times leads to a descent according to the law $y = -\frac{1}{2} gt^2$, which is in accord with the numerically calculated $\hat{y}(x, t)$ for small x.

The steady state potential $\Psi(z)$ also provides an estimate of how the shape of the Rayleigh–Taylor spike changes at large times. The motion of the interface is given by

$$\partial_t \hat{y}(x, t) = v_y - v_x \hat{y}_x(x, t). \tag{A.15}$$

Near the tip of the spike, $\hat{y}(x, t)$ can be expanded in a power series,

$$\hat{y} = -\tfrac{1}{2} gt^2 + \tfrac{1}{2} R^{-1}(t)\, x^2 + O(x^4), \tag{A.16}$$

with $R(t)$ denoting the radius of curvature at the tip. Substituting Eqs. (A.14) and (A.15) into (A.16), we infer for the coefficient of x^2,

$$\partial_t(R^{-1}) = 3R^{-1}/t.$$

This implies, for large t,

$$R(t) \approx \frac{\text{constant}}{t^3}. \tag{A.17}$$

ACKNOWLEDGMENTS

Useful discussions with Raymond Mjolsness and David Sharp at the early stages of this work are gratefully acknowledged.

REFERENCES

1. G. N. WHITE, Los Alamos National Laboratory report, LA-5575-MS, 1974 and "Geofluid Dynamical Wave Mathematics," Applied Mathematical Group, p. 54, Univ. of Washington, Seattle, 1977; M. S. LONGUET-HIGGINS AND E. D. COKELET, *Proc. R. Soc.* (London) A364, 1 (1978).
2. G. I. TAYLOR, *Proc. Roy. Soc. London Ser. A* **201** (1950), 192.
3. D. I. MEIRON, S. A. ORSZAG, AND M. ISRAELI, *J. Comput. Phys.* **40** (1981), 345.
4. G. R. BAKER, D. I. MEIRON, AND S. A. ORSZAG, *Phys. Fluids* **23** (1980), 1485.
5. R. MENIKOFF AND C. ZEMACH, *J. Comput. Phys.* **36** (1980), 366.
6. L. F. SHAMPINE AND M. K. GORDON, "Computer Solutions of Ordinary Differential Equations: The Initial Value Problem," Freeman, San Francisco, 1974.
7. P. G. SAFFMAN, *Arch. Mech.* **26** (1974), 423.
8. F. B. HILDEBRAND, "Introduction to Numerical Analysis," McGraw–Hill, New York, 1956.
9. R. M. DAVIES AND G. I. TAYLOR, *Proc. R. Soc. London Ser. A* **200** (1950), 375.
10. R. D. RICHTMYER, *Commun. Pure Appl. Math.* **13** (1960), 297.
11. K. A. MEYER AND P. J. BLEWETT, *Phys. Fluids* **15** (1972), 753.
12. I. TADGBAKHGH AND J. B. KELLER, *J. Fluid Mech.* **8** (1960), 422.
13. G. G. STOKES, "Considerations Relative to the Greatest Height of Oscillatory Irrotational Waves" *in* "Mathematical and Physical Papers," Vol. 1, P. 225, Cambridge Univ. Press, London/New York, 1880; L. W. SCHWARTZ, *J. Fluid Mech.* **62** (1974), 533.
14. G. BIRKHOFF AND D. CARTER, *J. Math. Mech.* **6** (1957), 769.
15. P. R. GARABEDIAN, *Proc. Roy. Soc. London Ser. A* **241** (1957), 423.